



Article

Temperature/Emissivity Separation of Typical Grassland of Northwestern China Based on Hyper-CAM and Its Potential for Grassland Drought Monitoring

Pengfei Liu ¹, Hongyuan Huo ^{2,*} , Li Guo ³, Pei Leng ⁴ and Long He ¹¹ College of Geography and Environmental Sciences, Tianjin Normal University, Tianjin 300393, China² Faculty of Architecture, Transportation and Civil Engineering, Beijing University of Technology, Beijing 100124, China³ Institute of Geospatial Information, Information Engineering University, Zhengzhou 450123, China⁴ Institute of Agricultural Resources and Regional Planning, Chinese Academy of Agricultural Sciences, Beijing 100081, China

* Correspondence: huohongyuan@bjut.edu.cn

Abstract: Research on grassland monitoring based on temperature/emissivity separation based on hyperspectral thermal infrared (HTIR) remote sensing is rare. Based on the longwave TIR instrument (Hyper-CAM), this study designed two experiments to collect HTIR datasets, separate the temperature and emissivity of different vegetation of grassland, and analyze the relationship between the emissivity of vegetation and soil moisture content. First, we collected the HTIR remotely sensed dataset of different kinds of vegetation and used the temperature/emissivity separation algorithm to separate the temperature and emissivity of seven types of vegetation. The temperature and emissivity of these types of vegetation were separated. Then, the absorption characteristics of the emissivity spectral curves of each type of grass were analyzed. The distribution and differences of the temperature and specific emissivity in different parts of these seven grassland vegetation types were quantitatively analyzed, and the relationship between their changes and vegetation leaf moisture and vegetation health status was also analyzed. Second, to monitor the drought of grassland vegetation, a second experiment was designed to measure the changes in the emissivity under different soil water contents. This observation experiment took *Artemisia frigida* as the research object. From the results of the separation of the temperature and emissivity, we found that the emissivity of *Artemisia frigida* has significantly changed with the increase in the water content, and the emissivity showed an overall increasing trend. We also quantitatively analyzed the differences in the temperature and specific emissivity between *Artemisia frigida* and *Artemisia subulata Nakai*, both belonging to the genus *Artemisia*, under different water content conditions. The overall waveform characteristics and their similarities and differences at 850–1280 cm⁻¹ were compared and analyzed. The experimental results show that Hyper-CAM can effectively obtain the emissivity of various types of grassland vegetation as the absorption characteristics of grassland vegetation in the thermal infrared spectral region were quite notable, which shows the significant potential ability of identification and discrimination of different types of grassland vegetation.

Keywords: temperature retrieval; spectral emissivity; soil moisture; water content; drought monitoring; grassland remote sensing



Citation: Liu, P.; Huo, H.; Guo, L.; Leng, P.; He, L. Temperature/Emissivity Separation of Typical Grassland of Northwestern China Based on Hyper-CAM and Its Potential for Grassland Drought Monitoring. *Remote Sens.* **2022**, *14*, 4809. <https://doi.org/10.3390/rs14194809>

Academic Editor: Ernesto López-Baeza

Received: 21 July 2022

Accepted: 19 September 2022

Published: 26 September 2022

Publisher's Note: MDPI stays neutral with regard to jurisdictional claims in published maps and institutional affiliations.



Copyright: © 2022 by the authors. Licensee MDPI, Basel, Switzerland. This article is an open access article distributed under the terms and conditions of the Creative Commons Attribution (CC BY) license (<https://creativecommons.org/licenses/by/4.0/>).

1. Introduction

Water-deficit stress, also known as water stress or drought stress, is one of the most important abiotic stress factors influencing vegetation growth, crop production, and food production quality [1–4]. The traditional method used to monitor vegetation health is the use of a meteorological dataset. Point-to-point monitoring is not representative of largescale monitoring. Remote sensing is capable of quickly and effectively extracting the

physiological, biochemical, and structural characteristics of crops from different platforms (including ground, air, and satellite) at the spatio-temporal scale and is not destructive [5–8]. In particular, hyperspectral remote sensing images with continuous spectral data can provide the possibility of detecting the relationship between spectral characteristics and plant growth status [9,10]. Hyperspectral remote sensing methods used to detect the relationship between vegetation spectral characteristics and vegetation growth mainly include solar-induced fluorescence remote sensing (SIF) [11–13], visible and near infrared short-wave infrared remote sensing (VNIR-SWIR), and thermal infrared (TIR) hyperspectral remote sensing [14–16].

Research on the detection of water stress based on chlorophyll-induced fluorescence remote sensing uses the chlorophyll fluorescence emission peaks centered at 670 and 760 nm to monitor the actual photosynthetic functional status of crops and detect crop responses to environmental stress. SIF is therefore a direct indicator of photosynthetic efficiency [17]. Research on SIF for vegetation water stress has been carried out on different experimental platforms [17–21]. SIF remote sensing requires an extremely high signal to noise ratio (SNR), which in turn limits the spectral or spatial resolution of the sensor. In addition to this limitation, fluorescence emission peaks appear in two ultra-narrow spectral window regions (e.g., around 670 and 760 nm), which requires nano-scale hyperspectral resolution technology. Despite the many challenges, the potential of SIF remote sensing for vegetation water stress is significant, which can also be inferred from the FLEX (Fluorescence Detector) satellite mission supported by the European Space Agency (ESA) [20].

The detection of water stress based on VNIR and SWIR remote sensing is mainly based on the spectral reflectance characteristics of vegetation leaves, canopy, and soil [22,23]. This spectrum is mainly focused on the electromagnetic spectrum reflection interval ranging from 0.4 to 2.5 μm . Typical sensors include Analytical Spectral Devices (ASDs) Field Spec.; Spectral Evolution Portable Spectro Radiometer (PSR)+; sensors on-board aviation platforms such as Airborne Visible/Infrared Imaging Spectrometer (AVIRIS), Hyperspectral Mapper (HyMap), Hyper Spectro Expo (HySpex), and ESPA Augmented Geostationary Laboratory Experiment (EAGLE); and sensors on-board satellites such as Landsat thematic mapper (TM)/enhanced thematic mapper (ETM), Satellite pour l'Observation de la Terre (SPOT), Moderate-resolution Imaging Spectroradiometer (MODIS), Hyperion, and other application platforms of different scales. Recently, many scientists have developed different vegetation indexes (VIs) to detect plant water stress based on the VNIR / SWIR spectrum interval, but most of them are based on an empirical relationship under specific experimental conditions and are therefore affected and limited by different plant species and environmental conditions [24]. These VIs include the water index (WI) moisture stress index (MSI), and leaf water index (LWI) [16,25,26]. However, these vegetation indices, to some extent, have lag effects in the monitoring of vegetation growth status, that is, the changes in these VIs are based on an obvious lack of water in the vegetation or obvious yellowing or withering of the leaves. Therefore, for early stress monitoring of vegetation moisture, these indexes have significant limitations and disadvantages.

Since the 1970s, thermal infrared remote sensing (8–14 μm) technology has been considered as a potential tool for early detection of water stress in vegetation. Generally, the emitted radiation in thermal infrared remote sensing (TIR) mainly contains two kinds of information: (i) the surface temperature and (ii) the spectral emissivity of the research object. Therefore, research on water stress detection based on thermal infrared remote sensing can be divided into water stress monitoring based on temperature and water stress monitoring based on spectral emissivity.

Temperature-based remote sensing water stress detection is the measurement of the leaf or canopy temperature to detect the plant's response to water stress [27,28]. The theory starts from the leaf energy balance equation, that is, the leaf temperature changes with the (evaporation) transpiration rate of the leaves, so the leaf temperature is a function of the stomatal conductance [29–31]. A series of vegetation indices have been developed based on the leaf or canopy temperature. Jackson (1977) and Idso (1977b) first proposed the study

of vegetation's daily stress degree (SDD) based on the relationship between vegetation temperature and space temperature [32,33]. Thermal indices based on stomatal conductance such as the crop water stress index (CWSI) and water deficit index (WDI) provide technical means for early detection of water stress in vegetation remote sensing [34,35].

Because the temperature-based index is only a relative indicator for plant stress monitoring and has no actual physical meaning, a physical-based evapotranspiration model can not only detect the plant's response to a water deficit but also further understand the plant's role in the exchange between the soil circle and the atmosphere circle under environmental stress. Mallick et al. (2015) provided a physical-based model method, namely the Surface Temperature Initiated Closure (STIC) method, which calculates evapotranspiration from the surface temperature retrieved by remote sensing [36]. The STIC method integrates the surface temperature into the Penman–Monteith (PM) equation.

Recently, the temperature-based monitoring method for vegetation water stress is generally based on a single broadband TIR channel ranging from 8 to 14 μm [37–45]. The use of broadband TIR thermal infrared remote sensing data to retrieve the surface temperature of the target vegetation is based on the assumption of a constant emissivity (for example, the emissivity of the vegetation is assumed to be 0.97). A 1% error in emissivity will result in an absolute temperature error of about 1K [27]. However, in reality, this assumption does not hold because it will reduce the accuracy of temperature estimation [46]. It is estimated that a 1% error in emissivity will result in an absolute temperature error of about 1 K [27].

Research on water stress detection in vegetation based on the spectral emissivity retrieved from hyperspectral thermal infrared remote sensing is rare. Most research on spectral emissivity measurements has been carried out in the laboratory. For example, Salisbury (1986) used directional hemispherical reflection (DHR) to measure and identify changes in the emissivity spectrum of the fresh leaves of 13 different tree species in the laboratory [47]. da Luz (2007) investigated the relationship between the spectral characteristics of vegetation emissivity and leaf compounds such as cellulose, xylan, lignin, cutin, and silica [15]. da Luz (2010) measured the emissivity of a vegetation canopy for the first time in the field [48].

As mentioned above, the temperature-based monitoring method based on a single broadband TIR channel will result in a large error, and it is difficult for the spectral emissivity-based method measured in the laboratory to meet the needs of practical remote sensing applications. With the development of hyperspectral thermal infrared technology, hyperspectral thermal infrared sensors such as Hyper-CAM have begun to be used in commercial applications. The previous literature shows that grassland remote sensing is mainly based on the VNIR spectral region to monitor grassland yield, grassland vegetation coverage, and grassland vegetation growth, with research on grassland emissivity measurement based on thermal infrared remote sensing rare. In this paper, based on the laboratory platform of hyperspectral thermal infrared remote sensing, Hyper-CAM, two experiments were designed to obtain the spectral emissivity of different kinds of grassland vegetation to quantify their spectral emissivity characteristics and analyze the relationship between the spectral characteristics and the soil water content.

2. Test Area

The test area is located in Baiyinkulun Ranch, Xilinhot, Inner Mongolia, northern China. Baiyinkulun Nature Reserve is located 80 km south of Xilinhot City, Xilinguole League, Inner Mongolia Autonomous Region, with coordinates of $116^{\circ}07'–116^{\circ}20'E$, $43^{\circ}13'–43^{\circ}17'N$, and an average elevation of 1294 m. It is adjacent to Keshiketeng Banner in the east, Abaga Banner in the west, Zhenglan Banner in the south, and Belek Ranch and Baiyinxile Ranch in the north. The total area of the ranch is 1257 km^2 , of which the Hunshandak sandy land area is 386 km^2 and the terrace area is 871 km^2 . Of the total area, grassland occupies about 1169.8 km^2 , woodland is about 35.3 km^2 , water is about 1.3 km^2 , crop land is 42.7 km^2 , and other area is 8 km^2 .

Baiyinkulun pastoral area belongs to a typical semi-arid continental climate. It is dry and rainless, with severe and long winters, short and cool summers, and windy and dry springs and autumns. There are many types of habitats around it, and plant species are abundant. There are both wet and aquatic plants that grow in swamps or lakes, and there are *xerophytes* and *mesophytes* that grow on sandy land. There are meadows of *Achnatherum splendens* of which herbs (e.g., *Achnatherum Splendens*) are the major dominant species in the community composition, and there are also *Salix pentandra* meadows of which short shrubs are the major dominant species (e.g., *Salix Pentandra*) in the community composition. There are both artificial *Populus davidiana* forests in man-made habitats and *Carex* meadows rich in wet plants; there are both typical steppe that are often damaged by locusts due to drought and mountain steppe meadows with clear community structures.

According to Table 1, it can be seen that the proportion of the cosmopolitan distribution if plant species in the three habitats of typical grassland, *Salix Pentandra* meadow, and *Achnatherum Splendens* meadow accounts for more than 80% of all species in this habitat. Pan-tropical-distributed plant species account for a very small proportion of all species in these three habitats, all of which are below 10%. This proportion of pan-tropical-distributed plant species is zero in the *Salix Pentandra* meadow and *Achnatherum Splendens* meadow. The proportion of temperate-distributed plant species to all species in these habitats is between the former two but with large changes. Among them, *Liliaceae*, *Leguminosae*, *Gramineae*, *Asteraceae*, and *Chenopodiaceae* are species in all 6 habitats; *Primulaceae*, *Agropyronceae*, and *Juniperaceae* are species unique to the *Carex* meadow. *Urticaceae*, *Euphorbiaceae*, and *Rutaceae* are species unique to typical grasslands. *Gentianaceae*, *Malvaceae*, *Crassulaceae*, and *Birch* are species unique to sandy land. *Solanaceae*, *White Flower Danaceae*, and *Sangkeae* are species unique to the artificial *Populus* forest.

Table 1. The proportion of plant species in different distribution areas accounting for all kinds of habitat distributions in Baiyinkulun area.

Habitat Distribution Types	Cosmopolitan	Pantropic	Temperate
Plant Species Types			
Carex Meadow	70.8%	4.2%	20.8%
Typical Steppe	85%	5%	10%
Sandy Vegetation	69.2%	7.7%	23.1%
Artificial <i>Populus Davidiana</i> Forests	75%	10%	15%
<i>Salix Pentandra</i> Meadow	82.4%		7.6%
<i>Achnatherum Splendens</i> Meadow	87.5%		12.5%

The distribution pattern of the Baiyinkulun plant family is mainly a world-wide and temperate distribution type, which is closely related to the temperate semi-arid continental climate zone where Baiyinkulun is located. Among the 41 families around Baiyinkulun Lake, *Liliaceae*, *Leguminosae*, *Gramineae*, *Compositae*, and *Chenopodiaceae* are the most widely distributed and common families while the tropical distribution type *Rubiaceae* has a narrow distribution range. Except for the artificial aspen forest, which uses trees as the constructive species, the other habitats are all herbaceous. The characteristics of the naturally growing plant flora in this area are obviously manifested in that the constructive species play a major role but still maintain a certain influence over the zonal grassland flora, that is, with the expansion of urbanization and the increase in human activities, the effect of the natural plant will be further significantly reduced.

3. Specification of Hyper-CAM

The Hyper-CAM Long Wavelength was designed as a lightweight and compact hyperspectral imaging instrument based on Fourier transfer infrared (FTIR) technology, which can be used to yield high spectral resolution remotely sensed data by enabling high-

accuracy radiometric calibration (see Figure 1). The Hyper-Cam features a focal-plane array (FPA) detector containing 320×256 pixels over a basic $6.4^\circ \times 5.1^\circ$ field-of-view (FOV). The FOV can be adjusted according to the specific application and corresponding request. The spectral resolution is between 0.25 and 150 cm^{-1} over the spectral range from 8 to $12 \mu\text{m}$. The Hyper-Cam offers high sensitivity for each pixel of the scene under observation, a single sweep noise equivalent spectral radiance (NESR) at $10 \mu\text{m}$ with a 128×128 window, and a spectral resolution of 16 cm^{-1} at $24.1 \text{ nW cm}^{-2} \text{ sr}^{-1} \text{ cm}^{-1}$. The spectral range of the sensor, which is defined as the spectral range where the NESR is 5 times better than the NESR at $10 \mu\text{m}$, ranges from 7.8 to $12 \mu\text{m}$. Moreover, its lightweight nature makes it ideal for field operation (see Figure 2). Table 2 is the main technical parameter of Hyper-CAM.

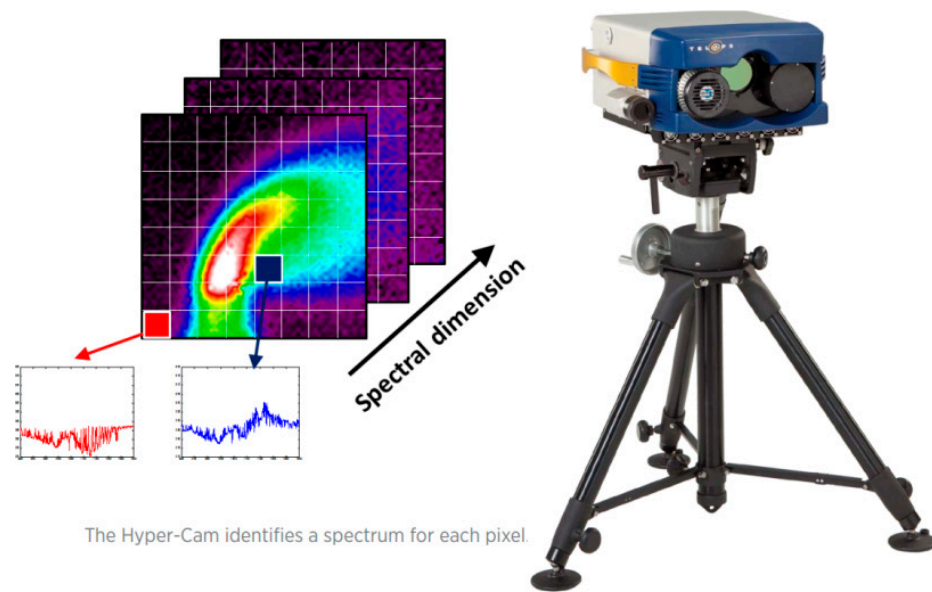


Figure 1. Picture of the long-wavelength Hyper-CAM instrument.

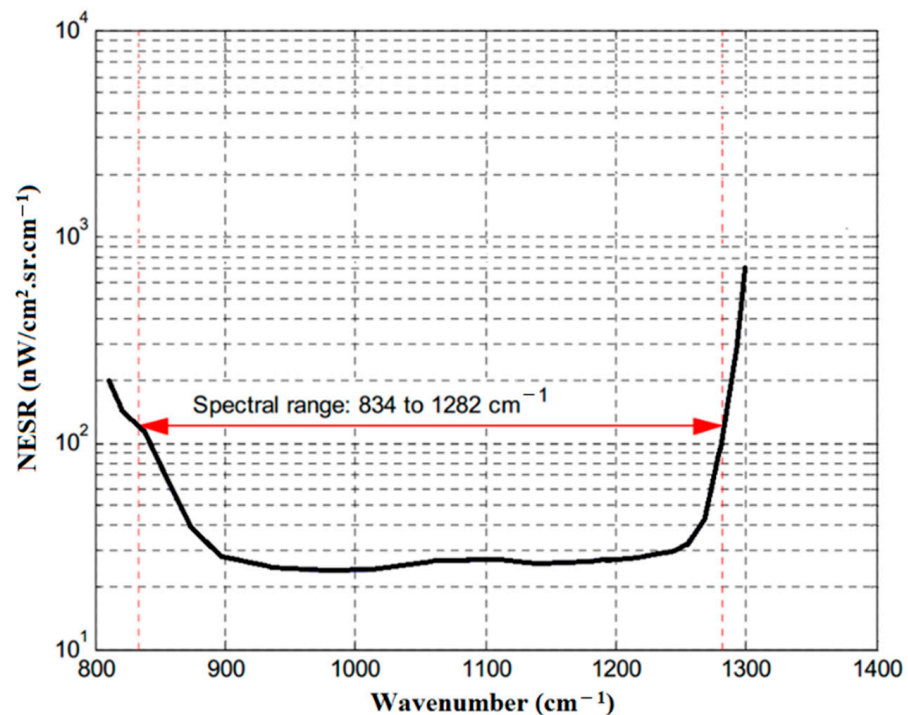


Figure 2. Spectral NESR measurement, averaged for all the good pixels.

Table 2. Technical parameters of Hyper-CAM.

Parameters	Unit	Mini.	Typical	Max.
Spectral range	μm	8		11
Spectral resolution	cm^{-1}	0.25	4	150
Spatial resolution	pixels		320×256	
Single beam FOV	Mrad		0.35	
Noise equivalent	$\text{nW}/\text{cm}^2 \text{ sr cm}^{-1}$		25 at 10 μm	
Radiometric accuracy	K		<1	
Commucation	Ethernet 10/100 Mbps		Ethernet 10/100 Mbps	
Data transfer			Cameral Link	
Detector cooling			Closed Cycle	
Weight	kg		27	

4. Methodology and Experiments

4.1. Temperature/Emissivity Separation Algorithm for Hyper-CAM Dataset

The temperature/emissivity was separated based on the iterative spectrally smooth temperature/emissivity separation (ISSTES) method (Borel 2008, Huo 2019). Due to the differences in the period of molecular vibrational excited states in solids and gases, the thermal infrared specific emissivity spectra of the former are significantly smoother than those of the latter. Therefore, the ground-object specific emissivity spectrum is generally smoother than the atmospheric spectrum. The Iterative Spectrally Smooth Temperature-Emissivity Separation algorithm takes the prior knowledge of the radiance spectrum as the constraint condition of the underdetermined inversion problem of the separation of the temperature and radiance. The retrieval accuracy fundamentally depends on the strength of the prior condition and has an important relationship with its regularization penalty function (Borel 2008). Using the ISSTES method to retrieve the surface temperature, the first step is to convert the raw interferograms into a spectral radiance dataset. Then, the surface temperature is retrieved using a solid TES method based on the spectral smoothness from the spectral radiances datasets. The state-of-the-art TES method allows for down-welling radiance (DWR) correction and is most suited for outside field measurement. The measurement of the spectral radiance and the derivation of the spectral emissivity and temperature in the field are processes that must be carried out carefully and thoughtfully. For the down-welling radiance (DWR), which was measured using the Infragold standard, according to the smoothness of the ISSTES method, the temperature and the emissivity are retrieved.

The main steps are as follows:

(1) Temperature/emissivity separation. The long wave infrared (LWIR) spectral radiance measured at the sensor can be written as:

$$L(\lambda) = \varepsilon(\lambda)B(\lambda, T)\tau(\lambda) + (1 - \varepsilon(\lambda))L^\downarrow(\lambda) + L^\uparrow \quad (1)$$

where λ is the wavelength, $B(\lambda, T)$ is the radiance of the blackbody at temperature T , $\tau(\lambda)$ is the transmission, $L^\downarrow(\lambda)$ is the down-welling radiance, and $L^\uparrow(\lambda)$ is the up-welling radiance. Solve Equation (1) for the spectral emissivity ε of the target yields at the ground:

$$\varepsilon = \left(L(\lambda) - L^\downarrow(\lambda) \right) / \left(B(\lambda, T_{est}) - L^\downarrow(\lambda) \right) \quad (2)$$

where the estimated ground temperature T_{est} is given by:

$$T_{est} = B^{-1}(\lambda_0, (L(\lambda) - (1 - \varepsilon_0))/\varepsilon_0) \quad (3)$$

where λ_0 is a wavelength (typically $\lambda_0 = 10.1 \mu\text{m}$) where the atmosphere is highly transmissive, and emissivity is typically set to $\varepsilon_0 = 0.95$.

(2) The down-welling radiance is the energy incident on the InfraGold diffuse reflectance standard, and it can be calculated from:

$$L^{\downarrow}(\lambda) = \left(L_{\text{InfraGold}}(\lambda) - \varepsilon_{\text{InfraGold}}(\lambda) L_{\text{BB}}(T_{\text{InfraGold}}, \lambda) \right) / (1 - \varepsilon_{\text{InfraGold}}) \quad (4)$$

where $\varepsilon_{\text{InfraGold}}$ is the flat spectral emissivity of *InfraGold* with a magnitude approximately equal to 0.04 (see Figure 3). $L_{\text{InfraGold}}$ and $T_{\text{InfraGold}}$ can be directly measured. The atmospheric effects are removed based on the calculated downwelling radiance. The *InfraGold* is measured when each grassland is measured by the Hyper-Cam instrument. Figure 3 shows the hemispherical reflectance of the *InfraGold* plate, which was designed as it was manufactured.

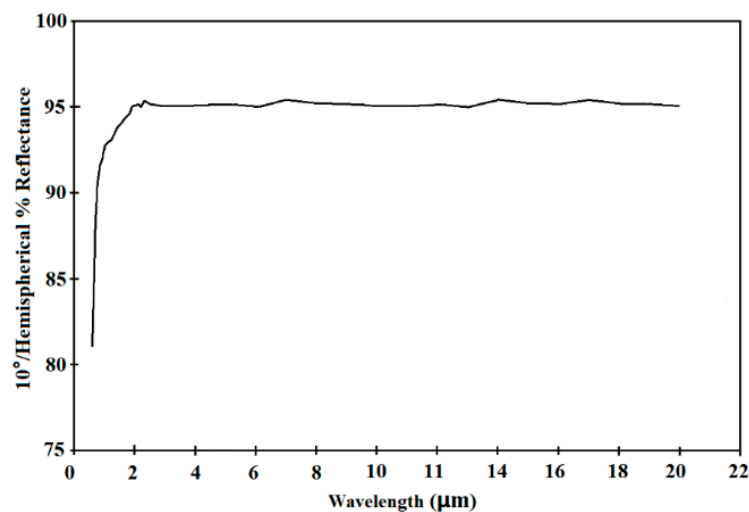


Figure 3. Hemispherical reflectance of the $\varepsilon_{\text{InfraGold}}$ plate.

(3) Find the smoothest emissivity. For the n -th spectral emissivity $\varepsilon_{n,m}$ with M samples, the smoothness is computed by:

$$\sigma(\varepsilon_n) = STDEV(\varepsilon_{n,m} - (\varepsilon_{n,m-1} + \varepsilon_{n,m} + \varepsilon_{n,m+1})/3) \quad (5)$$

where $m = 2, \dots, M - 1$, the emissivity with the smallest standard deviation $\sigma(\varepsilon_n)$ is chosen as the spectrally smoothest emissivity.

4.2. Experimental Design and Collection of Datasets

In this paper, two experiments were designed. The goals of these two experiments were (1) to acquire the hyperspectral thermal infrared image of the grass under clear sky conditions to separate the land surface temperature (LST) and specific emissivity of typical grassland of Inner Mongolia using the ISSTES algorithm; (2) obtain the specific emissivity of vegetation of at least three different species of grassland; (3) compare and analyze the changes in the specific emissivity of vegetation of different species and the characteristics of specific emissivity; and (4) taking vegetation as an example, conduct soil moisture control experiments to obtain observation data of vegetation under different soil moisture conditions, separate the emissivity and temperature of each type of grassland, and analyze the corresponding changes in different soil moisture conditions.

4.2.1. Experiment 1

The start of the first experiment was carried out on 22, Autumn, 2018, and the time for observation was midday, ranging from 10 AM to 15 PM under cloud-free conditions. In this experiment, a highly diffuse reference target (*InfraGold*, Labsphere Inc, North Sutton, NH, USA) of known reflectance was used and centered in the scans to quantify the downwelling radiance (DWR), and Hyper-Cam measurements were performed at the same time. The

Fluke TIR (see Figure 4) thermometer was used to measure the surface temperature of the InfraGold, and the atmospheric DWR was calculated according to the Planck function. The atmospheric effects were removed based on the calculated downwelling radiance (see Equations (1) to (4)). The InfraGold was measured when each grassland was measured by the Hyper-Cam instrument.

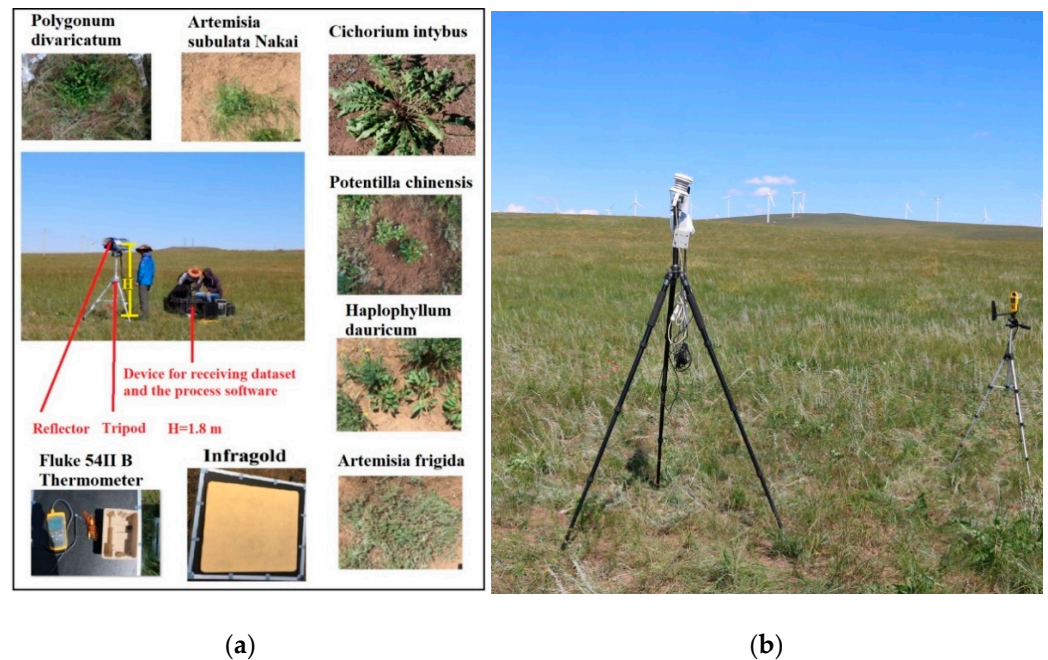


Figure 4. The experiments: (a) is the observation experiments of different types of vegetation, (b) is a simple meteorological station instrument for collecting the local climate data.

Figures 4 and 5 show the observation experiments and the targets of different vegetation types. The equipment for the field experiments mainly included the long-wave radioactive spectral instrument Hyper-CAM, a reflector, a tripod, a device for receiving the datasets and the processing software, and a generator to provide a stable power supply for normal operation of the instrument. In the period from 21 to 25 Autumn, 2018, two field experiments for retrieval of the emissivity of different types of grassland and detection of their changes with the water variation were conducted on typical grassland under controlled conditions at the Baiyinkulun Nature Reserve.



Figure 5. Photo of *Artemisia subulata Nakai*.

Observation Targets

According to the previous observations, the research objects were identified as several species commonly found in the Baiyinkulun Ranch in Xilinhot. The observation targets mainly included *Polygonum divaricatum* of the genus *Polygonum* of the family *Polygonaceae*, *Artemisia frigida* and *Artemisia subulata* of the Nakai of genus *Artemisia* of the family *Compositae*, *Cichorium intybus* of the genus *Cichorium* of the family *Compositae*, *Stipa capillata* of the genus *Stipeae* of the family *Gramineae*, *Haplophyllum dauricum* of the genus *Haplophyllum* of the family *Rutaceae*, and *Potentilla chinensis* of the genus *Potentilla* of the family *Rosaceae*. These types of grasses are common and widely distributed in local grasslands.

Artemisia subulata Nakai

Artemisia subulata Nakai (*Artemisia subulata* Nakai) is a perennial herb of the genus *Artemisia* in the *Compositae* family (see Figure 5). The roots are thin, and the lateral roots are few; the rhizomes are thin, with many upright vegetative branches. It is a perennial herb. The roots are thin, and the lateral roots are few; the rhizomes are thin, creeping, with multiple upright vegetative branches. The stems are few or solitary, 45–80 cm high, with thin longitudinal ribs, lavender or brown; some branches or the upper half of the stem have short and upward branches with inflorescence. The stems and branches are slightly pilose at the beginning, and then glabrous. It flowers and fruits from August to October. *Artemisia sylvestris* mostly grows in low-altitude humid and semi-humid areas such as hillsides, forest edges, river banks, swamp edges, and meadows.

Polygonum divaricatum

Polygonum divaricatum (*Polygonum divaricatum*) is a perennial herb of the family *Polygonum* (see Figure 6). The stem is upright, 70–120 cm high, glabrous, branched from the base, branches are forked and spread, and the plant appearance is spherical. The leaves are lanceolate or oblong, 5–12 cm long, 0.5–2 cm wide, sharply pointed at the apex, wedge-shaped or narrowly wedge-shaped at the base, usually with short ciliate edges, and glabrous or sparsely pilose on both sides. The petiole is about 0.5 cm long. The stipules are membranous, oblique, 1–2 cm long, sparsely pilose or glabrous, cracked, and shed. The inflorescence is paniculate and branched. Flowering occurs from July to August and fruiting occurs from August to September.



Figure 6. Photo of *Polygonum divaricatum* from Baiyinkulun Grassland.

Haplophyllum dauricum

Haplophyllum dauricum is a perennial herb of the *Rutaceae* family and the genus *Ruta* (see Figure 7). The underground part of the stem is quite strong and woody, and the above-ground part has many stems and branches, and the plant height can reach 50 cm. The leaves are thick and papery, with slender branchlets. The leaves are narrowly lanceolate to linear, with pointed ends, usually oblanceolate or obovate, and gray-green. The midrib is inconspicuous.



Figure 7. Photo of *Haplophyllum dauricum* from Baiyinkulun Grassland.

Potentilla chinensis

Potentilla (*Potentilla chinensis*) is a perennial herb belonging to the *Rosaceae* and *Potentilla* genus (see Figure 8). The roots are strong, cylindrical, and slightly lignified. The flower stems are erect or ascending, 20–70 cm high, sparsely pubescent, and white silky pilose. The basal leaves are pinnately compound leaves, with 5–15 pairs of leaflets, separated by 0.5–0.8 cm, and the petiole is 4–25 cm long. The petiole is pubescent and silky pilose. The leaflets are opposite or alternate, the upper leaflets are longer, and gradually decrease downwards. The basal leaf stipules are nearly membranous, brown, with a white silky pilose outside, and the stem leaf stipules are herbaceous and green, with sharply cracked edges.



Figure 8. Photo of *Potentilla chiesnsis* from Baiyinkulun Grassland.

Cichorium intybus

Chicory (*Cichorium intybus* L.) belongs to the genus *Asteraceae* and is a perennial herb with a height of 40–100 cm (see Figure 9). Roots are short and thick. Stems are erect, ribbed, hollow, and much branched. Leaves alternate and are long oblanceolate. Basal leaves are rosette-shaped and petioles attenuate at the base, 15–34 cm long and 2–4 cm wide. The base is attenuated and has a stipe, the margin is sparsely serrated, and there are 3–6 pairs of lateral lobes. The top lateral lobes are larger and all lateral lobes are sickle-shaped or irregularly sickle-shaped or triangular. All leaves are thin in texture, with sparse multicellular long-node hairs on both sides but more hairs on the veins and edges.



Figure 9. Photo of *Cichorium intybus* from Baiyinkulun Grassland.

Stipa capillata

Stipa (scientific name: *Stipa capillata* L.) is a perennial dense bush herb of the family *Poaceae* and *Stipa* (see Figure 10). Culms are erect, tufted, 40–80 cm high, often with 4 nodes, with persistent dead leaf sheaths at the base. Leaf sheaths are smooth or slightly rough, longer than internodes. For *Ligule-lanceolate*, the basal ones are 1–1.5 mm long and the culm-born ones are 4–8 mm long. The leaves are longitudinally rolled into a linear shape, hairy above and rough below, and the basal leaves are up to 40 cm long.



Figure 10. Photo of *Stipa capillata* from Baiyinkulun Grassland.

Observation Target: *Artemisia frigida*

Artemisia frigida (*Artemisia frigida*) is a perennial herb of the *Compositae* genus *Artemisia*, sometimes slightly subshrub-like (see Figure 11). Several or most of the stems are often clustered, sparsely solitary, 10–70 cm high, and densely covered with gray or light-yellow silk hairs. The rhizome grows horizontally, with many adventitious roots, and is lush. The base of the stem is woody, the leaves are short-stalked or sessile, and both sides are densely covered with gray or light-yellow silky hairs. The middle leaves are oblong or obovate-ovate, 0.5–0.7 cm long, one to two pinnately split, each with 3–4 side lobes, and the middle and upper side lobes are often split 3–5. The upper leaves and bracts are pinnately split or split 3–5. The flowering period is August–September. It is widely distributed in the grassland belt and desert grassland belt. It is the main component of grassland subshrubs.



Figure 11. Photo of *Artemisia frigida* from Baiyinkulun Grassland.

4.2.2. Experiment 2

In order to explore and analyze the potential of hyperspectral thermal infrared remote sensing data in grassland vegetation drought monitoring, a study was carried out on the emissivity change in grassland vegetation under different moisture conditions. We chose *Artemisia annua*, which is more common in Baiyinkulen Ranch, as the research object. The reason for choosing *Artemisia annua* is that the *Artemisia annua* plant is relatively short and covers a wide range of ground and grows densely. The shortness and density of the plant determine that it is less affected by wind than other vegetation, and the wide growth range is more convenient for measurement. The day before the measurement experiment, *Artemisia annua* was watered, and at 10 am the next day, the soil water content of *Artemisia annua* was measured by the Time-Domain-Reflectometry (TDR), and then the hyperspectral thermal infrared remote sensing data was collected by Hyper-CAM. Figure 12 shows *Artemisia annua*. The three parts A/B/C surrounded by the red line in the figure are the areas of no watering, less watering, and more watering, respectively. The soil moisture contents (SMCs) measured by TDR were 7.4%, 12.5%, and 20.1%, respectively.

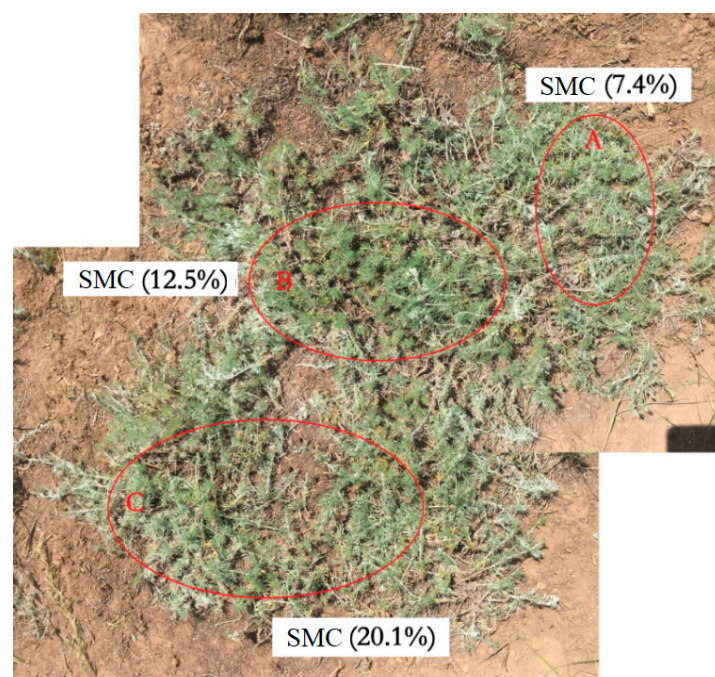


Figure 12. Observation experiment of *Artemisia frigida* with different SMCs.

5. Results and Discussion

5.1. Research on the Characteristics of the Emissivity Curves of Different Types of Grassland Vegetation Based on Experiment 1

5.1.1. Temperature and Emissivity Retrieval of *Haplophyllum dauricum*

Figure 13 shows the schematic diagram of *Haplophyllum dauricum* and the surface temperature retrieved based on Hyper-CAM hyperspectral thermal infrared remote sensing data. In the temperature image, the texture structure of *Haplophyllum dauricum* is relatively clear, which also reflects the healthy growth state of the plant. The leaf area of northern rue is small, and the texture of the stem and so on is clear in the temperature image. It can also be seen from the temperature image that the leaf temperature of *Haplophyllum dauricum* is relatively uniform, and the difference between the leaf temperature and the stem diameter temperature is small. The petal temperature was slightly different from the leaf temperature, possibly due to the difference in the water content between the leaves and petals. In addition, its temperature image is quite different from that of the neighboring *Potentilla chinensis*, and its temperature value was relatively low. Through observation, it was found that the leaf thickness of these two plants is different, and the difference in the leaf structure may lead to a large difference in the leaf water content of these two plants. Figure 14 shows the down-welling radiance retrieved from the gold-plate and the emissivity spectrum of *Haplophyllum dauricum*. It can be seen from the figure that there is a strong emission front at 877 cm^{-1} and a strong emission valley at 887 cm^{-1} . Then, there are two consecutive small emission fronts at 892 and 904 cm^{-1} , and weaker emission valleys at 949 , 977 and 987 cm^{-1} . There are relatively weak absorption characteristics at 1050 and 1180 cm^{-1} , and strong absorption characteristics at 1135 , 1170 , and 1210 cm^{-1} .

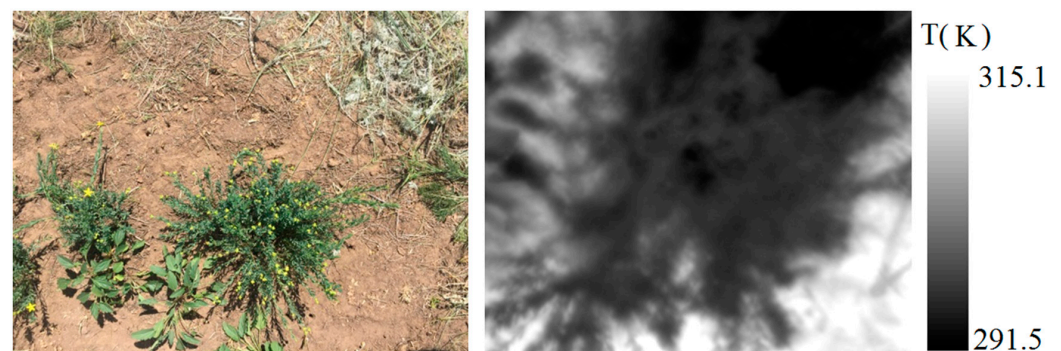


Figure 13. Temperature of *Haplophyllum dauricum* retrieved from the HTIR dataset.

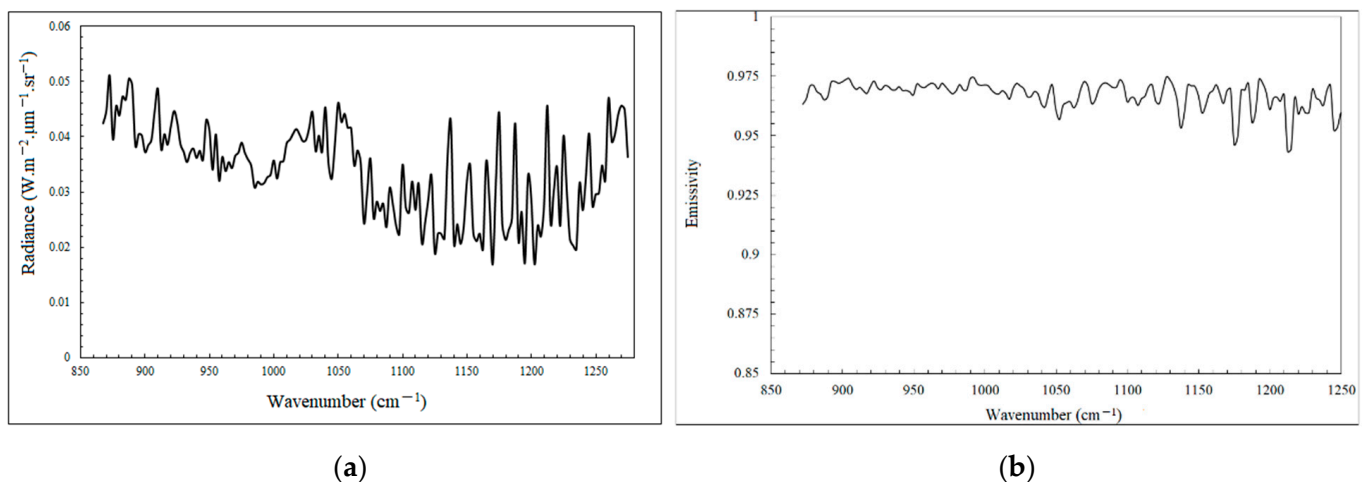


Figure 14. Results of emissivity retrieval and the down-welling radiance. (a) is the down-welling radiance retrieved from the gold-plate, and (b) the emissivity of *Haplophyllum dauricum*.

5.1.2. Temperature and Emissivity Retrieval of *Artemisia subulata Nakai* and *Stipa capillata*

Figure 15 shows a schematic diagram of *Artemisia subulata Nakai* and *Stipa capillata* and the leaf surface temperature retrieved based on the hyperspectral thermal infrared remote sensing data acquired by Hyper-CAM. Compared with the temperature image of *Stipa capillata*, the texture structure of the temperature image of *Artemisia subulata Nakai* is more clearly distinguishable, which also reflects the superior cold resistance of *Artemisia subulata Nakai*. In addition, the temperature image distribution of *Artemisia subulata Nakai* appears less uniform when compared to that of *Stipa capillata*. The closer to the center of the leaves, the lower the temperature, and the temperature image of *Stipa capillata* shows that the leaves and stems are basically the same, which is related to their own texture structure, because *Artemisia subulata Nakai* leaves are narrower and thicker and its spatial texture is relatively uniform. The overall temperature of *Artemisia subulata Nakai* was lower than that of *Stipa capillata*, possibly because the leaves of *Artemisia subulata Nakai* are thicker than *Stipa capillata*, and thus, it may store more water than *Stipa capillata*.

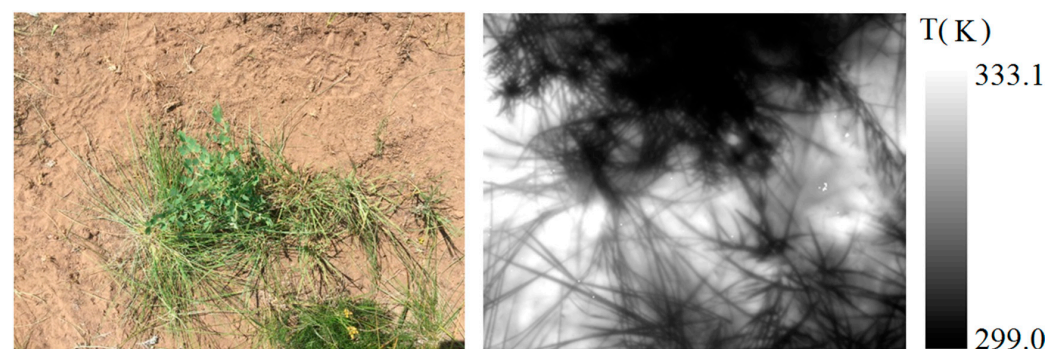


Figure 15. Temperature of *Artemisia subulata Nakai* retrieved from the HTIR dataset.

Figure 16 shows the down-welling radiance retrieved from gold-plate and the emissivity curves of *Artemisia subulata Nakai* and *Stipa capillata* based on the inversion of HTIR data observed by Hyper-CAM. It can be seen from the figure that *Artemisia subulata Nakai* has some absorption characteristics in the thermal infrared spectral range, such as weak absorption characteristics at 920, 930, 953, and 970 cm^{-1} , and obvious absorption characteristics around 1040, 1060, 1105, 1170, 1190, and 1215 cm^{-1} , and the absorption width is narrower than that of *Stipa capillata*. *Stipa capillata* has strong emission fronts near 879, 902, 927, 964, 1017 and 1042 cm^{-1} . There are relatively strong absorption valleys around 887, 909, and 949 cm^{-1} . This is followed by three continuous absorption valleys at 1004, 1029, and 1054 cm^{-1} , and three wider emission fronts at 1097, 1124 and 1202 cm^{-1} .

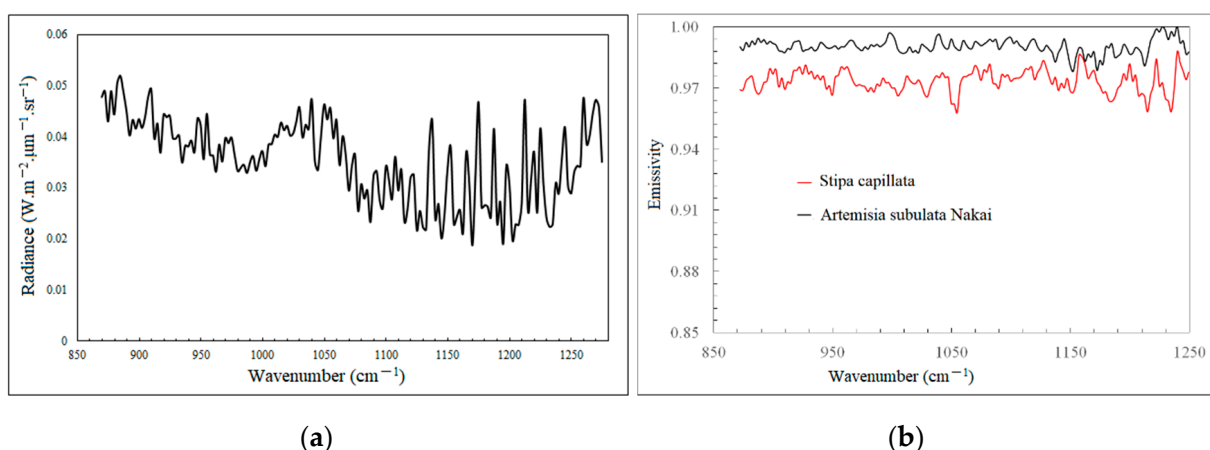


Figure 16. Results of emissivity retrieval and the down-welling radiance. (a) is the down-welling radiance retrieved from the gold-plate and (b) the emissivity of *Artemisia subulata Nakai* and *Stipa capillata*.

5.1.3. Temperature and Emissivity Retrieval of *Potentilla chinensis*

Figure 17 shows a schematic diagram of *Potentilla chinensis* and its leaf surface temperature image obtained by inversion, which actually contains two vegetation types, namely *Potentilla chinensis* and *Haplophyllum dauricum*. It can also be seen from the temperature image that the temperature distribution of *Potentilla chinensis* is actually the same as that of *Haplophyllum dauricum*, and the closer to the center, the lower the temperature. In addition, it can also be found that *Potentilla chinensis* and its background temperature differences are smaller than that of *Haplophyllum dauricum*, which may be mainly due to the different physiological structures of the two vegetations (such as different leaf thickness and leaf tissue structure). It can also be seen from the temperature image that the temperature of the leaves in different parts of *Potentilla chinensis* varies greatly. Some yellowing and aged leaves closer to the root were warmer while the top leaves of *Potentilla chinensis*, which were further away from the root, were more tender and had cooler leaves. In addition to changes in the physical structure, differences in the water content may also be another factor affecting this difference.



Figure 17. Temperature of *Potentilla chinensis*.

Figure 18 shows the down-welling radiance retrieved from the gold-plate and the emissivity image of *Potentilla chinensis* obtained based on Hyper-CAM inversion. It can be seen from the figure that the emissivity of *Potentilla chinensis* has weak absorption characteristics at 890, 905, 925, and 1025 cm^{-1} , and at 1050, 1070, and 1100 cm^{-1} , it has obvious absorption characteristics of the second order. Relatively strong absorption features were observed at 1135, 1150, 1170, 1200, 1210 and 1225 cm^{-1} .

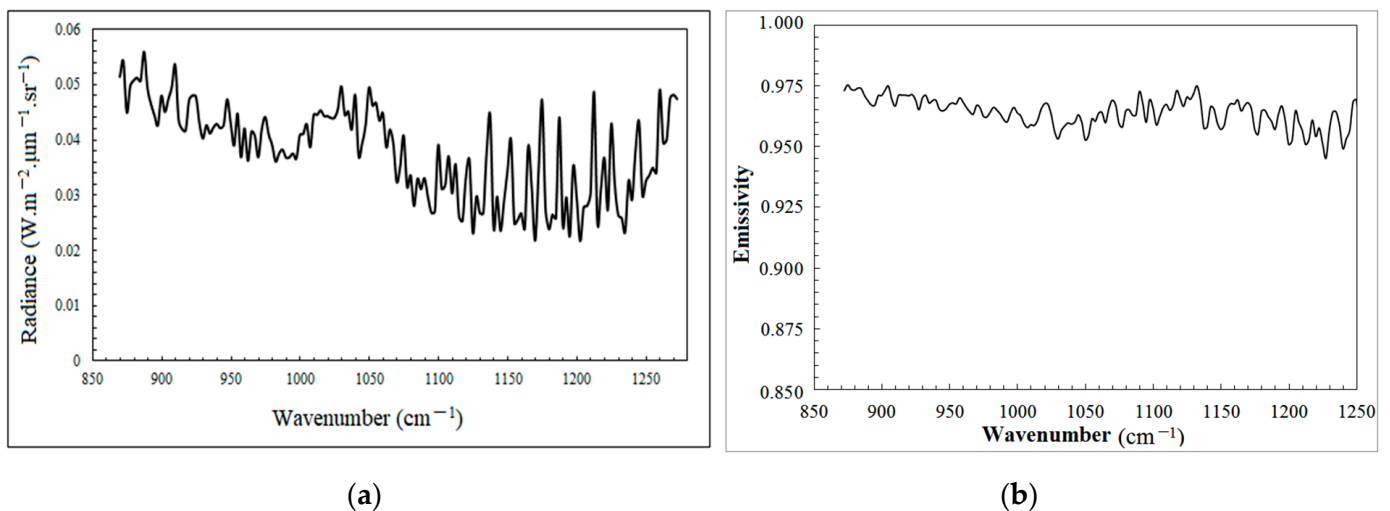


Figure 18. Results of emissivity retrieval and the down-welling radiance. (a) is the down-welling radiance retrieved from the gold-plate and (b) the emissivity of *Potentilla chinensis*.

5.1.4. Temperature and Emissivity Retrieval of *Cichorium intybus*

Figure 19 shows the field photograph of *Cichorium intybus* and the temperature image of the whole *Cichorium intybus* observed by Hyper-CAM. The leaf morphology, spatial texture, and canopy structure of *Cichorium intybus* can be seen in the image. From the temperature image, it can be found that the brightness near the central stem of *Cichorium intybus* is darker and the brightness of the leaves is lighter, so the temperature near the stem is lower than that of the leaves, the thickness of the leaves of the chicory is uniform, and the temperature difference of the same leaf is not obvious. The temperature of the central rod and the diameter of different blades are also inconsistent, indicating that the water content of different rod diameters is also different, and the temperature values of different blade parts on the same rod diameter are also different. It also shows that the water content of different blade parts from the center of the rod diameter is slightly different.

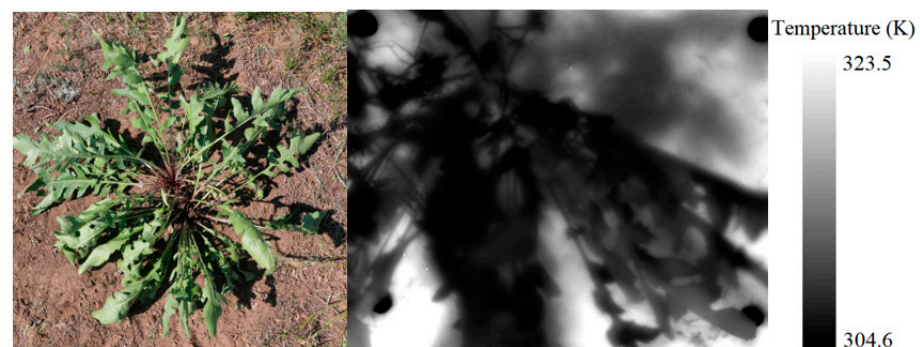


Figure 19. Temperature of *Cichorium intybus*.

Figure 20 is the down-welling radiance retrieved from the gold-plate and the emissivity curve of *Cichorium intybus* based on HyperCAM observation and inversion. It can be seen from the figure that there is a weaker emission wind near 879 cm^{-1} and a weaker and narrower emission valley near 884 cm^{-1} . Then, there are four emission peaks in decreasing order in the vicinity of $897, 922, 947,$ and 972 cm^{-1} . There are two absorption valleys at 912 and 934 cm^{-1} , followed by two continuous absorption valleys at 1004 and 1007 cm^{-1} . Four narrow and strong absorption valleys can be observed near $1049, 1094, 1137,$ and 1172 cm^{-1} , and three relatively sharper and stronger fronts can be found around $1082, 1104,$ and 1204 cm^{-1} , respectively.

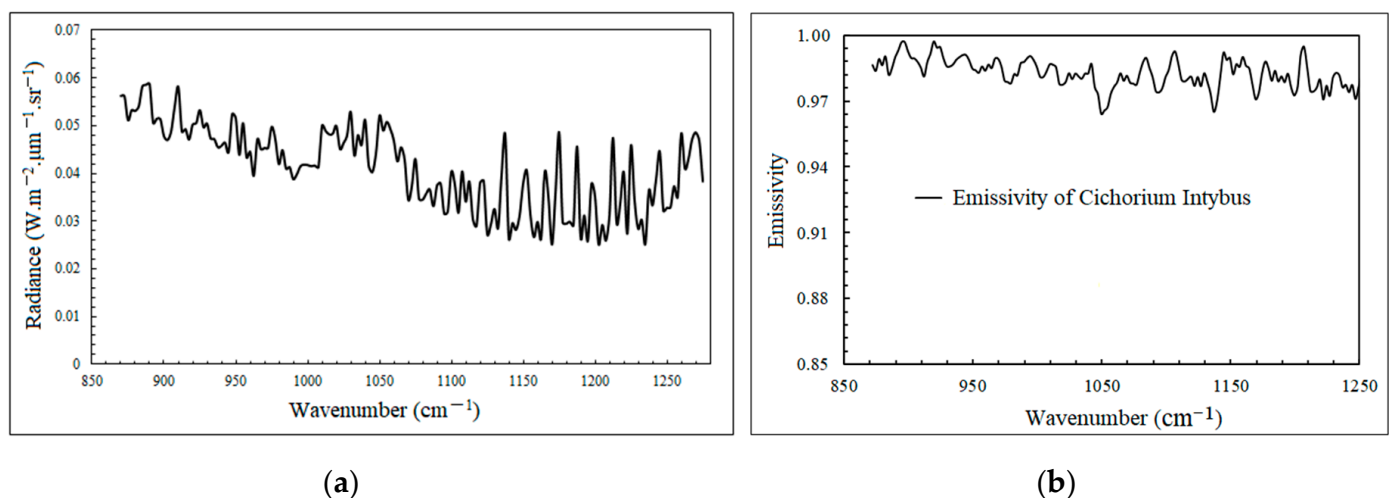


Figure 20. Results of emissivity retrieval and the down-welling radiance. (a) is the down-welling radiance retrieved from the gold-plate, and (b) the emissivity of *Cichorium intybus*.

5.1.5. Temperature and Emissivity Retrieval of *Polygonum divaricatum*

Figure 21 is a schematic diagram of the *Polygonum divaricatum* vegetation and its leaf temperature image as observed by Hyper-CAM. The leaf morphology and canopy structure of *Polygonum divaricatum* can be clearly seen from the image. Therefore, *Polygonum divaricatum* has good growth conditions, a uniform temperature distribution, and a small temperature difference on the same leaf. Due to the structural factors of *Polygonum divaricatum* leaves, it can be seen in the image that the temperature in the middle of the leaves is slightly lower, and the temperature at the edges is relatively slightly higher. Compared with the other types of vegetation mentioned above, the leaf area of *Polygonum divaricatum* is larger and thinner, and the overall temperature difference of the leaves is smaller.

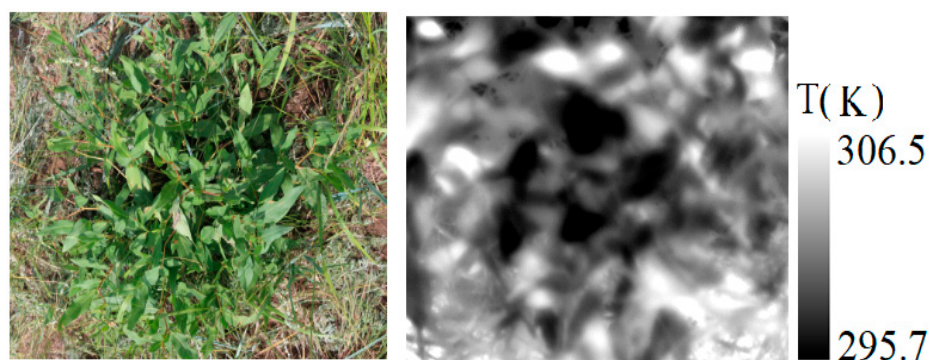


Figure 21. Temperature of *Polygonum divaricatum*.

Figure 22 shows the radiance image obtained based on Hyper-CAM observation and the emissivity curves of *Polygonum divaricatum*. It can be seen from the figure that there are weak emission peaks at 887, 917, 939, and 962 cm^{-1} , and relatively weak emission peaks near 892, 924, and 944 cm^{-1} . There are five continuous relatively strong absorption valleys near 1014, 1032, 1052, 1082, and 1102 cm^{-1} . However, there are relatively strong and broad emission peaks at 1169, 1192, and 1239 cm^{-1} . There is a weak and narrow emission peak at 1129 cm^{-1} , and two strong and narrow emission peaks at 1207 and 1247 cm^{-1} .

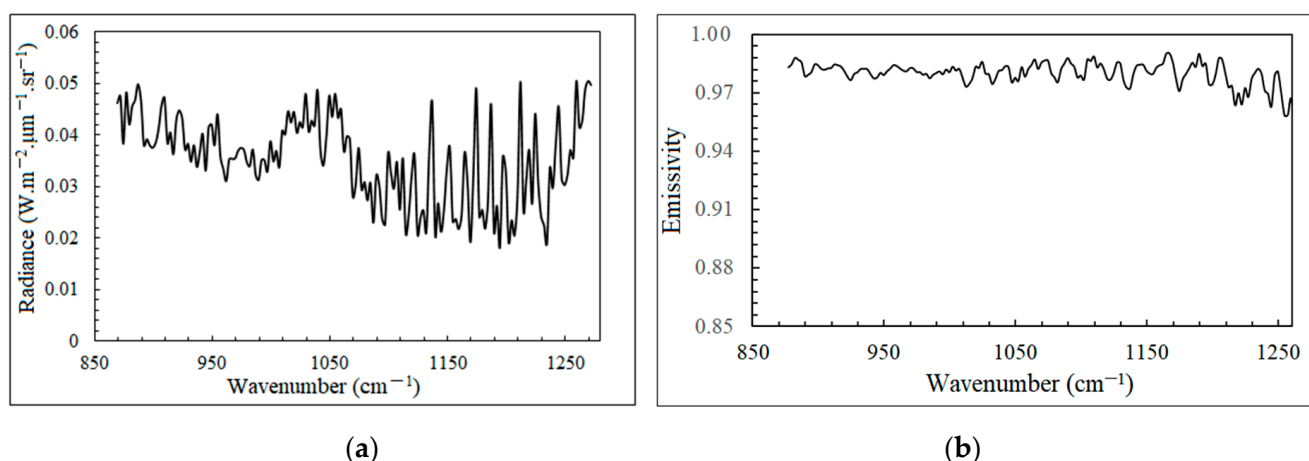


Figure 22. Results of emissivity retrieval and the down-welling radiance. (a) is the down-welling radiance retrieved from the gold-plate, and (b) the emissivity of *Polygonum divaricatum*.

5.2. Characteristic Changes in the Emissivity of *Artemisia annua* under Different Moisture Conditions Based on Experiment 2

Figure 23 shows a schematic diagram of *Artemisia frigida*. It consists of three parts, namely no watering (A), less watering (B), and more watering (C). The soil moisture content measured by TDR is 20.1%, 12.5%, and 7.4%, respectively. The image on the right is the surface temperature of *Artemisia frigida* retrieved based on Hyper-CAM's hyperspectral

thermal infrared remote sensing data. It can be seen from the figure that, except for the soil background value, the temperature distribution of *Artemisia frigida* vegetation in area A is uniform, and the temperature difference is small. The temperature difference of *Artemisia frigida* in area B is more obvious and the temperature difference of *Artemisia frigida* in area C is the largest, and the distribution is not even.

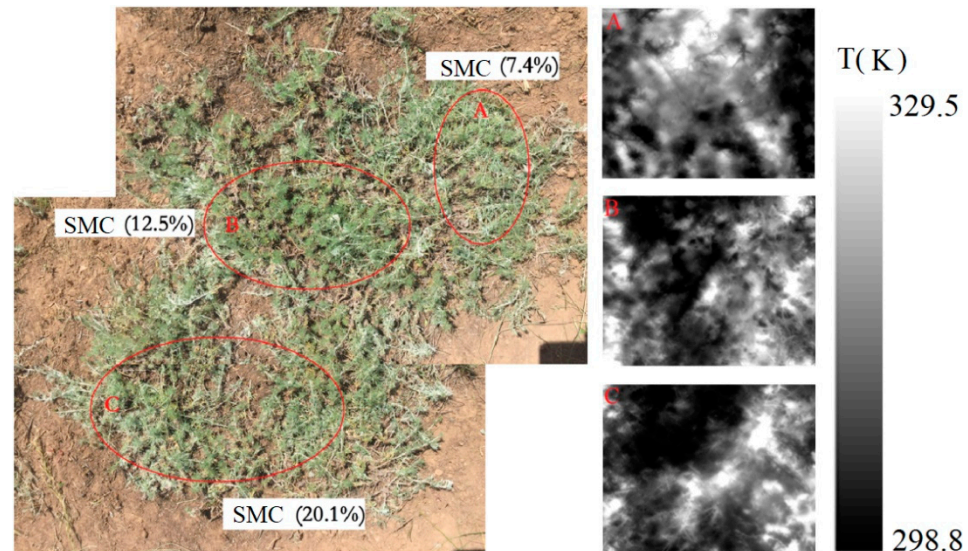


Figure 23. Temperature of *Artemisia frigida*.

Figure 23 shows the emissivity curve of *Artemisia frigida* obtained by inversion of the surface temperature and specific emissivity based on the data observed by the Hyper-CAM hyperspectral thermal infrared imager. The three curves shown in A, B, and C correspond to *Artemisia frigida* in the three different soil water content regions in Figure 24 respectively. It can be seen from the figure that the overall spectral shapes of the three emissivity curves A, B, and C are basically similar. However, there are obvious differences in their detailed characteristics, such as inconsistencies at 920, 970, and 1050 cm^{-1} . With the increase in the soil water content, the emission fronts near 880 cm^{-1} moves to a short wave, which are 877 (A), 882 (B), and 884 cm^{-1} (C), respectively. The two continuous absorption valleys around 982 and 992 cm^{-1} shift to long waves with increasing soil water content. The specific emissivity curve absorption characteristics of *Artemisia frigida* are mainly manifested at 877, 904, 912, 940, 982, 992, 1020, 1054, 1120, 1170, 1210, and 1225 cm^{-1} .

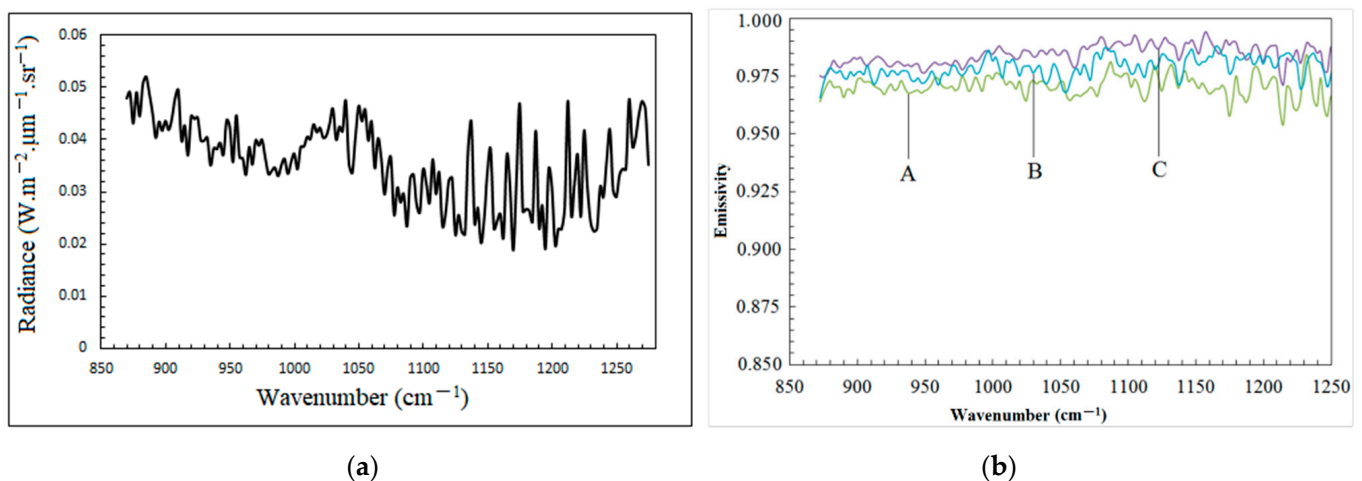


Figure 24. Results of emissivity retrieval and the down-welling radiance. (a) is the down-welling radiance retrieved from the gold-plate, and (b) the emissivity of *Artemisia frigida*.

Comparing the temperature and specific emissivity curves of *Artemisia subulata Nakai* and *Artemisia frigida*, with both belonging to the genus *Asteraceae*, we found that they have obvious diagnostic spectral characteristics in the range of 1100 to 1250 cm^{-1} . The fluctuation change in the emissivity curve in the range of 1000 to 1070 cm^{-1} is relatively small. There are weak diagnostic characteristic bands from 850 to 1000 cm^{-1} . Comparing the emissivity curve of *Artemisia frigida* without water and the emissivity curve of *Artemisia subulata Nakai*, we also found that the mean of the overall emissivity curve of *Artemisia subulata Nakai* is higher than that of *Artemisia frigida*. This may be attributed to the lower leaf water content of *Artemisia frigida* and *Artemisia subulata Nakai* under the conditions measured at the time. Comparison of the temperature images can also illustrate this problem because the mean leaf temperature of *Artemisia subulata Nakai* is lower than that of *Artemisia frigida*.

6. Conclusions and Suggestions

Grassland in northern China has serious ecological and environmental problems (such as serious grassland desertification) due to drought, and early warning of grassland drought is necessary. The traditional monitoring methods based on meteorological stations have poor generality and representativeness and cannot meet the practical needs. Drought monitoring research based on remote sensing mostly focuses on some index factors (such as NDVI, TDVI, etc.) that indirectly indicate drought developed in the visible-near-infrared interval. The temperature information related to drought can be directly obtained in the thermal infrared remote sensing range, so drought monitoring based on thermal infrared remote sensing has advantages that other remote sensing methods do not have.

This study was based on the above-mentioned starting point and based on the laboratory Hyper-CAM hyperspectral thermal infrared remote sensing sensor platform. Two experiments were designed to obtain the hyperspectral thermal infrared observation data of different types of vegetation in the grassland in the experimental area. Based on the hyperspectral thermal infrared surface temperature and specific emissivity separation algorithm, which were used to perform vegetation surface temperature inversion and emissivity separation, we obtained temperature images and emissivity images of seven types of vegetation of four different species. The uniformity of the leaf temperature of each type of vegetation and the difference in the leaf temperature distribution of vegetation of the same species were analyzed. The absorption characteristics of the emissivity of each type of plants were significantly different, and the absorption characteristics of the emissivity of the same species (such as *Artemisia frigida* and *Artemisia subulata Nakai*) were also quite different.

In order to detect drought in early grassland vegetation, it is necessary to measure the emissivity of vegetation under different soil water content conditions. Therefore, this study designed a second experiment. Taking *Artemisia frigida* of Compositae as the research object, the water control experiment was carried out on *Artemisia frigida* with appropriate amounts of water, and the specific emissivity of *Artemisia frigida* under different soil water content conditions was observed. Through the experiments, we found that the emissivity of *Artemisia frigida* changed significantly with the increase in the water content, and the difference in its detail absorption characteristics was more obvious, and the emissivity increased as a whole.

Through the experiments, we found that: (1) Hyperspectral thermal infrared remote sensing can be used to effectively identify and classify vegetation of different types and species in grasslands; (2) thermal infrared remote sensing can be used as an effective means for grassland dry detection; (3) the emissivity of typical vegetation types of grassland can be obtained based on Hyper-CAM; and (4) the absorption characteristics of grassland vegetation in the thermal infrared spectral range are obvious and significant. Obtaining the emissivity of different grassland vegetation and building a typical grassland emissivity spectral library will provide effective support for grassland vegetation identification and drought monitoring in the future.

In this study, although the temperature and specific emissivity curves of several different types of grassland vegetation were obtained, and the relationship between the vegetation specific emissivity and soil water content was discussed, there is still much work to be carried out to achieve improvements. First, in terms of separating temperature/emissivity, hyperspectral thermal infrared remote sensing data has many bands, and the information redundancy between adjacent bands is high. Therefore, considering in-depth exploration of hyperspectral thermal infrared remote sensing information and improving the accuracy of temperature/emissivity separation is one of the important tasks to be considered in the future. Secondly, it is difficult to validate the separation results of grassland vegetation temperature and specific emissivity. Especially for vegetation with a small leaf area, it is more difficult to directly measure the temperature. In the future, it is an important direction for future work to use a group of instruments comprehensively to carry out multi-angle remote sensing inversion of the temperature of leaves, and verify the results of the temperature and carry out laboratory measurement of the emissivity. Third, further exploration of the relationship between specific emissivity and changes in soil water and leaf water contents is of great significance for monitoring vegetation health in future work.

Author Contributions: Conceptualization, H.H.; methodology, H.H.; software, H.H. and P.L. (Pengfei Liu); validation, H.H., L.G., P.L. (Pei Leng) and L.H.; formal analysis, H.H., P.L. (Pengfei Liu) and L.H.; investigation, H.H., P.L. (Pei Leng) and P.L. (Pengfei Liu); resources, H.H.; data curation, H.H.; writing—original draft preparation, H.H.; writing—review and editing, H.H.; visualization, H.H.; supervision, H.H., P.L. (Pengfei Liu) and P.L. (Pei Leng); project administration, H.H.; funding acquisition, P.L. (Pengfei Liu) and L.G. All authors have read and agreed to the published version of the manuscript.

Funding: This research and the APC were funded by the Scientific Research Project of Beijing Municipal Educational Commission (grant number KM202110005017) and by the National Natural Science of Foundation of China (grant number 41701425).

Data Availability Statement: Not applicable.

Conflicts of Interest: The authors declare no conflict of interest.

References

1. Chaves, M.M.; Pereira, J.S.; Maroco, J.; Rodrigues, M.L.; Ricardo, C.P.; Osório, M.L.; Carvalho, I.; Faria, T.; Pinheiro, C. How plants cope with water stress in the field? Photosynthesis and growth. *Ann. Bot.* **2002**, *89*, 907–916. [[CrossRef](#)] [[PubMed](#)]
2. Hopkins, W.G.; Huner, N.P.A. Responses of plants to environmental stresses. In *Introduction to Plant Physiology*; John Wiley & Sons, Inc.: Hoboken, NJ, USA, 2009; pp. 223–239.
3. Ni, Z.; Liu, Z.; Huo, H.; Li, Z.L.; Nerry, F.; Wang, Q.; Li, X. Early Water Stress Detection Using Leaf-Level Measurements of Chlorophyll Fluorescence and Temperature Data. *Remote Sens.* **2015**, *7*, 3232–3249. [[CrossRef](#)]
4. Ni, Z.; Huo, H.; Tang, S.; Li, Z.L.; Liu, Z.; Xu, S.; Chen, B. Assessing the response of satellite sun-induced chlorophyll fluorescence and MODIS vegetation products to soil moisture from 2010 to 2017: A case in Yunnan Province of China. *Int. J. Remote Sens.* **2019**, *40*, 2278–2295. [[CrossRef](#)]
5. Chaerle, L.; Van Der Straeten, D. Imaging techniques and the early detection of plant stress. *Trends Plant Sci.* **2000**, *5*, 495–501. [[CrossRef](#)]
6. Gebbers, R.; Adamchuk, V.I. Precision Agriculture and Food Security. *Science* **2010**, *327*, 828–831. [[CrossRef](#)]
7. Mulla, D.J. Twenty five years of remote sensing in precision agriculture: Key advances and remaining knowledge gaps. *Biosyst. Eng.* **2013**, *114*, 358–371. [[CrossRef](#)]
8. Huo, H.; Li, Z.L.; Xing, Z. Temperature/emissivity separation using hyperspectral thermal infrared imagery and its potential for detecting the water content of plants. *Int. J. Remote Sens.* **2019**, *40*, 1672–1692. [[CrossRef](#)]
9. Pinter, P.J., Jr.; Hatfield, J.L.; Schepers, J.S.; Barnes, E.M.; Moran, M.S.; Daughtry, C.S.T.; Upchurch, D.R. Remote Sensing for Crop Management. *Photogramm. Eng. Remote Sens.* **2003**, *69*, 647–664.
10. Ni, Z.; Lu, Q.; Huo, H.; Zhang, H. Estimation of Chlorophyll Fluorescence at Different Scales: A Review. *Sensors* **2019**, *19*, 3000. [[CrossRef](#)]
11. Ni, Z.; Liu, Z.; Li, Z.-L.; Nerry, F.; Huo, H.; Li, X. Estimation of solar-induced fluorescence using the canopy reflectance index. *Int. J. Remote Sens.* **2015**, *36*, 5239–5256. [[CrossRef](#)]
12. Ni, Z.; Liu, Z.; Li, Z.-L.; Nerry, F.; Huo, H.; Sun, R.; Yang, P.; Zhang, W. Investigation of Atmospheric Effects on Retrieval of Sun-Induced Fluorescence Using Hyperspectral Imagery. *Sensors* **2016**, *16*, 480. [[CrossRef](#)] [[PubMed](#)]

13. Zhao, L.; Liu, Z.; Xu, S.; He, X.; Ni, Z.; Zhao, H.; Ren, S. Retrieving the Diurnal FPAR of a Maize Canopy from the Jointing Stage to the Tasseling Stage with Vegetation Indices under Different Water Stresses and Light Conditions. *Sensors* **2018**, *18*, 3965. [[CrossRef](#)] [[PubMed](#)]
14. Rascher, U.; Alonso, L.; Burkart, A.; Cilia, C.; Zemek, F. Suninduced fluorescence—A new probe of photosynthesis: First maps from the imaging spectrometer HyPlant. *Glob. Chang. Biol.* **2015**, *21*, 4673–4684. [[CrossRef](#)] [[PubMed](#)]
15. da Luz, B.R.; Crowley, J.K. Spectral reflectance and emissivity features of broad leaf plants: Prospects for remote sensing in the thermal infrared (8.0–14.0 μm). *Remote Sens. Environ.* **2007**, *109*, 393–405. [[CrossRef](#)]
16. Seelig, H.-D.; Hoehn, A.; Stodieck, L.S.; Klaus, D.M.; Adams, W.W.; Emery, W.J. Relations of remote sensing leaf water indices to leaf water thickness in cowpea, bean, and sugarbeet plants. *Remote Sens. Environ.* **2008**, *112*, 445–455. [[CrossRef](#)]
17. Dechant, B.; Ryu, Y.; Badgley, G.; Zeng, Y.; Berry, J.A.; Zhang, Y.; Goulas, Y.; Li, Z.; Zhang, Q.; Kang, M.; et al. Canopy structure explains the relationship between photosynthesis and sun-induced chlorophyll fluorescence in crops. *Remote Sens. Environ.* **2020**, *241*, 111733. [[CrossRef](#)]
18. Meroni, M.; Rossini, M.; Guanter, L.; Alonso, L.; Rascher, U.; Colombo, R.; Moreno, J. Remote sensing of solar-induced chlorophyll fluorescence: Review of methods and applications. *Remote Sens. Environ.* **2009**, *113*, 2037–2051. [[CrossRef](#)]
19. Porcar-Castell, A.; Tyystjarvi, E.; Atherton, J.; van der Tol, C.; Flexas, J.; Pfundel, E.E.; Moreno, J.; Frankenberg, C.; Berry, J.A. Linking chlorophyll a fluorescence to photosynthesis for remote sensing applications: Mechanisms and challenges. *J. Exp. Bot.* **2014**, *65*, 4065–4095. [[CrossRef](#)]
20. Rossini, M.; Nedbal, L.; Guanter, L.; Ač, A.; Alonso, L.; Burkart, A.; Cogliati, S.; Colombo, R.; Damm, A.; Drusch, M. Red and far red Sun-induced chlorophyll fluorescence as a measure of plant photosynthesis. *Geophys. Res. Lett.* **2015**, *42*, 1632–1639. [[CrossRef](#)]
21. Wieneke, S.; Ahrends, H.; Damm, A.; Pinto, F.; Stadler, A.; Rossini, M.; Rascher, U. Airborne based spectroscopy of red and far-red sun-induced chlorophyll fluorescence : Implications for improved estimates of gross primary productivity. *Remote Sens. Environ.* **2016**, *184*, 654–667. [[CrossRef](#)]
22. Moran, M.S.; Inoue, Y.; Barnes, E.M. Opportunities and limitations for image-based remote sensing in precision crop management. *Remote Sens. Environ.* **1997**, *61*, 319–346. [[CrossRef](#)]
23. Govender, M.; Dye, P.; Weiersbye, I. Review of commonly used remote sensing and groundbased technologies to measure plant water stress. *Water SA* **2009**, *35*, 741–752. [[CrossRef](#)]
24. Jones, H.G.; Vaughan, R.A. *Remote Sensing of Vegetation : Principles, Techniques, and Applications*; Oxford University Press: Oxford, UK, 2010.
25. Hunt, E., Jr.; Rock, B. Detection of changes in leaf water content using Near- and Middle-Infrared reflectances. *Remote Sens. Environ.* **1989**, *30*, 43–54.
26. Peñuelas, J.; Gamon, J.A.; Fredeen, A.L.; Merino, J.; Field, C.B. Reflectance indices associated with physiological changes in Nitrogen- and water- limited sunflower leaves. *Remote Sens. Environ.* **1994**, *48*, 135–146. [[CrossRef](#)]
27. Jones, H.G. Application of Thermal Imaging and Infrared Sensing in Plant Physiology and Ecophysiology. In *Advances in Botanical Research*; Academic Press: Cambridge, MA, USA, 2004; pp. 107–163.
28. Tardy, B.; Rivalland, V.; Huc, M.; Hagolle, O.; Marcq, S.; Boulet, G. A software tool for atmospheric correction and surface temperature estimation of Landsat infrared thermal data. *Remote Sens.* **2016**, *8*, 696. [[CrossRef](#)]
29. Maes, W.H.; Steppe, K. Estimating evapotranspiration and drought stress with ground-based thermal remote sensing in agriculture: A review. *J. Exp. Bot.* **2012**, *63*, 4671–4712. [[CrossRef](#)]
30. Costa, J.M.; Grant, O.M.; Chaves, M.M. Thermography to explore plant-environment interactions. *J. Exp. Bot.* **2013**, *64*, 3937–3949. [[CrossRef](#)]
31. Maes, W.H.; Baert, A.; Huete, A.R.; Minchin, P.E.H.; Snelgar, W.P.; Steppe, K. A new wet reference target method for continuous infrared thermography of vegetations. *Agric. For. Meteorol.* **2016**, *226–227*, 119–131. [[CrossRef](#)]
32. Jackson, R.D.; Reginato, R.J.; Idso, S.B. Wheat canopy temperature: A practical tool for evaluating water requirements. *Water Resour. Res.* **1977**, *13*, 651–656. [[CrossRef](#)]
33. Idso, S.B.; Jackson, R.D.; Reginato, R.J. Remote sensing for agricultural water management and crop yield prediction. *Agric. Water Manag.* **1977**, *1*, 299–310. [[CrossRef](#)]
34. Moran, M.S.; Clarke, T.R.; Inoue, Y.; Vidal, A. Estimating crop water deficit using the relation between surface-air temperature and spectral vegetation index. *Remote Sens. Environ.* **1994**, *49*, 246–263. [[CrossRef](#)]
35. Jones, H.G. Use of thermography for quantitative studies of spatial and temporal variation of stomatal conductance over leaf surfaces. *Plant Cell Environ.* **1999**, *22*, 1043–1055. [[CrossRef](#)]
36. Mallick, K.; Boegh, E.; Trebs, I.; Alfieri, J.G.; Kustas, W.P.; Prueger, J.H.; Niyogi, D.; Das, N.; Drewry, D.T.; Hoffmann, L.; et al. Reintroducing radiometric surface temperature into the Penman-Monteith formulation. *Water Resour. Res.* **2015**, *51*, 6214–6243. [[CrossRef](#)]
37. Jones, H.G.; Serraj, R.; Loveys, B.R.; Xiong, L.; Wheaton, A.; Price, A.H. Thermal infrared imaging of crop canopies for the remote diagnosis and quantification of plant responses to water stress in the field. *Funct. Plant Biol.* **2009**, *36*, 978–989. [[CrossRef](#)] [[PubMed](#)]

38. Grant, O.M.; Davies, M.J.; James, C.M.; Johnson, A.W.; Leinonen, I.; Simpson, D.W. Thermal imaging and carbon isotope composition indicate variation amongst strawberry (*Fragaria × ananassa*) cultivars in stomatal conductance and water use efficiency. *Environ. Exp. Bot.* **2012**, *76*, 7–15. [[CrossRef](#)]
39. Leng, P.; Li, Z.-L.; Duan, S.-B.; Gao, M.-F.; Huo, H.-Y. First results of all-weather soil moisture retrieval from an optical/thermal infrared remote-sensing-based operational system in China. *Int. J. Remote Sens.* **2019**, *40*, 2069–2086. [[CrossRef](#)]
40. Pei, L.; Li, Z.-L.; Duan, S.B.; Tang, R.; Gao, M.-F. A method for deriving all-sky evapotranspiration from the synergistic use of remotely sensed images and meteorological data. *J. Geophys. Res. Atmos.* **2017**, *122*, 13–263.
41. Leng, P.; Li, Z.-L.; Duan, S.-B.; Gao, M.-F.; Huo, H.-Y. A practical approach for deriving all-weather soil moisture content using combined satellite and meteorological data. *ISPRS J. Photogramm. Remote Sens.* **2017**, *131*, 40–51. [[CrossRef](#)]
42. Li, Z.L.; Leng, P.; Zhou, C.; Chen, K.S.; Zhou, F.C.; Shang, G.F. Soil moisture retrieval from remote sensing measurements: Current knowledge and directions for the future. *Earth-Sci. Rev.* **2021**, *218*, 103673. [[CrossRef](#)]
43. Leng, P.; Liao, Q.Y.; Gao, M.F.; Duan, S.B.; Li, Z.L.; Zhang, X.; Shang, G.F. A full satellite-driven method for the retrieval of clear-sky evapotranspiration. *Earth Space Sci.* **2019**, *6*, 2251–2262.
44. Wang, Y.; Leng, P.; Ma, J.; Peng, J. A Method for Downscaling Satellite Soil Moisture Based on Land Surface Temperature and Net Surface Shortwave Radiation. *IEEE Geosci. Remote Sens. Lett.* **2022**, *19*, 3002105. [[CrossRef](#)]
45. Zarco-Tejada, P.J.; González-Dugo, V.; Williams, L.E.; Suárez, L.; Berni, J.A.; Goldhamer, D.; Fereres, E. 2013. A PRI-based water stress index combining structural and chlorophyll effects: Assessment using diurnal narrow-band airborne imagery and the CWSI thermal index. *Remote Sens. Environ.* **2013**, *138*, 38–50. [[CrossRef](#)]
46. Ullah, S.; Skidmore, A.K.; Naeem, M.; Schlerf, M. An accurate retrieval of leaf water content from mid to thermal infrared spectra using continuous wavelet analysis. *Sci. Total Environ.* **2012**, *437*, 145–152. [[CrossRef](#)] [[PubMed](#)]
47. Salisbury, J.W. Preliminary measurements of leaf spectral reflectance in the 8–14 μm region. *Int. J. Remote Sens.* **1986**, *7*, 1879–1886. [[CrossRef](#)]
48. da Luz, B.R.; Crowley, J.K. Identification of plant species by using high spatial and spectral resolution thermal infrared (8.0–13.5 μm) imagery. *Remote Sens. Environ.* **2010**, *114*, 404–413. [[CrossRef](#)]